

Kalman Filters for Air Data System Bias Correction for a Fixed-Wing UAV

Kasper Trolle Borup, Bård Nagy Stovner, Thor Inge Fossen, *Fellow, IEEE*, and Tor Arne Johansen, *Senior Member, IEEE*

Abstract—This paper presents two Kalman filter approaches for correcting air data systems providing relative velocity measurements with an additive constant or slowly time-varying bias for fixed-wing unmanned aerial vehicles (UAVs). In addition to the air data system, both estimators rely on a standard sensor suite consisting of a GNSS receiver, an IMU, and a heading reference. Furthermore, the estimators are based on kinematics and do not require a model of the UAV. The two estimators are in the noise-free case proven to have globally exponentially stable (GES) equilibrium points of the error dynamics if provided with persistence-of-excitation (PE) of the angular velocity of the UAV. The estimators are verified through simulation and using experimental flight data. The relative velocity measurements in the experimental flight results are provided by an array of pressure sensors embedded in the surface of the UAV combined with a neural network algorithm. The results indicate that a certain amount of PE is needed in order to have converging bias estimates for turbulent wind conditions.

Index Terms—Unmanned Aerial Vehicle, UAV, Air Data System Bias Correction, Air Data Estimation, Relative Velocity, Wind Velocity, Virtual Sensor, Airspeed, Angle of Attack, Sideslip Angle, Air Data Parameters, Fixed-Wing Aircraft, Flight Tests.

I. INTRODUCTION

Knowledge of the wind is very important in fixed-wing UAV control and operation. The relative velocity of the UAV with respect to the wind contains information from which the airspeed, angle of attack (AOA), and sideslip angle (SSA) are directly computable. The airspeed, AOA, and SSA are commonly referred to as the air data¹ and their values during flight are directly related to the performance and safety of the UAV. For beyond visual line of sight (BVLOS) operations, it is difficult for the pilots operating the UAV to reliably assess the wind on the aircraft, and it is therefore essential to have either a sensor system to measure the air data or algorithms to provide accurate estimates of them for these types of operations. The low speed and light weight of small to medium-sized UAVs make them susceptible to strong winds and the influence of the wind on the ground speed is not negligible. In order to have optimal path planning and UAV range estimates, it is necessary to have air data information [10, 24]. In addition, having air data knowledge, can open

up for more complex maneuvers such as high precision deep-stall landings [20], precision object delivery [19, 21], or for detecting critical performance degradation caused by ice accretion on the UAV due to atmospheric icing conditions [32].

The commercially available air data measurement solutions, commonly referred to as air data systems, are all based on a pneumatic multi-hole probe protruding from the UAV that is connected to a pressure scanner inside the UAV through rubber tubes. For example, the Aeroprobe Corporation solution, the Micro Air Data System [1], uses a 5-port air data probe connected to a pressure scanner. The pressure scanner contains a microcomputer that runs an algorithm to calculate air data parameters from the direct pressure measurements from the ports on the probe. The pressure scanner and the air data probes combined with the necessary wind tunnel tests needed to calibrate the system, result in a significant price compared to low-cost UAVs. The expensive components and the need for expensive calibration therefore limits the use of the air data systems in low-cost UAVs.

Several papers has been published on air data estimation for UAVs using a standard sensor suite consisting of an IMU, a GNSS receiver, a heading or attitude reference, and a Pitot-static probe providing airspeed measurements. Long and Song [18] used sensor fusion in a modular architecture where both an aerodynamic and kinematic model was used to estimate the AOA and airspeed. A Newton-Raphson solver on an aerodynamic model combined with an EKF, was proposed by Ramprasad and Arya [26] to obtain AOA and SSA estimates. Lie and Gebre-Egziabher [17] presented a cascaded EKF structure and an aircraft dynamics model for estimating the air data without the Pitot-static probe airspeed measurement. Cho et al. [8] proposed an EKF method that assumes a scaled measurement of the airspeed combined with an aerodynamic model of the system to estimate the AOA, the SSA, and the airspeed sensor scaling factor. Wenz et al. [34] used a simplified aerodynamic model for the lift force combined with the Dryden wind model (as described in [9]) in an EKF structure. Wenz and Johansen [33] built on this result with a moving horizon estimator and improved the accuracy. A common denominator for the preceding methods is the use of an aerodynamic model of the forces on the UAV. Aerodynamic forces are complex and a potential disadvantage of this approach is that model errors due to simplifications or parameter inaccuracies may result in estimation error. Johansen et al. [13] proposed a model-free

Kasper Trolle Borup, Bård Nagy Stovner, Professor Thor Inge Fossen, and Professor Tor Arne Johansen are with the Department of Engineering Cybernetics, Centre for Autonomous Marine Operations and Systems, The Norwegian University of Science and Technology, NO-7059 Trondheim, Norway, e-mail: kasper.borup@ntnu.no, bard.b.stovner@ntnu.no, thor.fossen@ntnu.no, and tor.arne.johansen@ntnu.no

¹Often the similarity parameters, the Mach number and Reynolds number, are also included.

kinematic approach for estimating the wind velocity and a Pitot-static tube scaling factor. The system was linear and Johansen et al. was able to show global exponential stability of the error dynamics equilibrium points under persistence of excitation of the aircraft. Rhudy et al. [28] presented a model-free nonlinear Kalman filter approach for estimating the airspeed without a Pitot-static probe by using wind vanes providing AOA and SSA measurements.

Research has also been conducted into employing an array of pressure sensors to estimate the air data parameters for fixed-wing aircraft. An extensive amount of research in flush air data sensing (FADS) systems originates from NASA in response to the problems associated with protruding Pitot probes. The FADS systems utilize pneumatic pressure orifices that are flush with the surface, placed in a symmetric and circular pattern on the nose of an aircraft combined with a aerodynamic pressure model. Larson et al. [15] demonstrated a FADS system in wind tunnels for subsonic airspeeds. Larson et al. extended this to transonic airspeeds [16], and Whitmore et al. [35] demonstrated the system in-flight. Using the FADS system in combination with neural networks (NNs) was proposed and demonstrated by Rohloff et al. [29, 30]. This approach was proposed for a soaring UAV by Quindlend and Langelaan [25]. Instead of pneumatic pressure sensors, Callegari et al. [6], showed that by combining a maximum likelihood estimator with strips of capacitive pressure sensors applied to the wings of a UAV, it was possible in simulation to estimate the airspeed and AOA. Samy et al. [31] developed a FADS system for a mini air vehicle where a matrix of pressure orifices was placed on the leading edge of the wing and a neural network was used to estimate the air data parameters. Borup et al. [5] proposed and demonstrated an air data system consisting of low-cost MEMS-based pressure sensors embedded in the surface of a UAV combined with machine learning algorithms. This system was used for the experimental flight test results in Section VII. However, the methods presented in this paper could be used for any air data system with a constant or slowly time-varying bias and the system presented [5] system was simply one example of such a system.

A. Contributions of this paper

The contributions of this paper are two distinct Kalman filter approaches for correcting an air data system or air data estimator with low-frequency drift or a constant error bias. If not mitigated, this drift or error bias can result in inaccurate measurements that potentially renders the system useless or even worse provides dangerous input to a control system. The low-frequency drift or constant bias errors could be due to sensor performance degradation, structural changes on the UAV or sensors, or from operating outside of the ambient conditions for which the system was calibrated for. Both presented estimators use only a standard sensor suite consisting of a GNSS receiver, an IMU, and a heading reference, combined with an air data system that is assumed to provide

biased relative velocity measurements. Provided with PE of the angular velocity of the UAV, the two linear time-varying systems are proven to be uniform completely observable (UCO) and uniform completely controllable (UCC), implying GES for the deterministic case and boundedness in the mean square sense for the stochastic case. Having two different estimators provides freedom in choosing the estimator that relies on the highest quality sensors. Furthermore, using both estimators in parallel potentially opens up for a fault detection and isolation structure such as presented by Ray and Luck [27]

B. Notation and preliminaries

For a vector or matrix X , X^\top denotes its transpose. The operator $\|\cdot\|$ denotes the Euclidean norm. For a vector $x \in \mathbb{R}^3$, $S(x)$ denotes the skew-symmetric matrix

$$S(x) = \begin{bmatrix} 0 & -x_3 & x_2 \\ x_3 & 0 & -x_1 \\ -x_2 & x_1 & 0 \end{bmatrix}$$

The $n \times n$ identity matrix is denoted by I_n and the $m \times n$ zero element matrix by $0_{m \times n}$. For the estimators presented in this paper, two different coordinate frames are considered, namely the body-fixed (BODY) frame and the North-East-Down (NED) frame. Vectors decomposed in the BODY and NED coordinate frames are denoted by the superscripts b and n , respectively. Consequently, the relation between a vector x^b decomposed in the BODY frame and its corresponding decomposition in the NED frame x^n , is governed by $x^n = R_b^n x^b$ where $R_b^n \in \text{SO}(3)$ is the rotation matrix from BODY to NED. Furthermore, we have the corresponding rotation matrix from NED to BODY as $R_n^b = (R_b^n)^\top$.

II. PROBLEM FORMULATION

The velocity over ground of a UAV can be expressed as the sum of the relative velocity and the wind velocity according to

$$v_g^n = R_b^n v_r^b + v_w^n \quad (1)$$

where $v_g^n = [v_n, v_e, v_d]^\top$ is the velocity over ground of the UAV decomposed in the NED frame, $v_r^b = [u_r, v_r, w_r]^\top$ is the relative velocity of the UAV with respect to the wind decomposed in the BODY frame and $v_w^n = [w_n, w_e, w_d]^\top$ is the wind velocity decomposed in the NED frame. The goal is to estimate either v_w^n or v_r^b , since knowledge of one allows computing the other using only known measurements. From the relative velocity the airspeed, AOA and SSA are found by

$$V_a = \sqrt{u_r^2 + v_r^2 + w_r^2} \quad (2)$$

$$\alpha = \tan^{-1} \left(\frac{w_r}{u_r} \right) \quad (3)$$

$$\beta = \sin^{-1} \left(\frac{v_r}{V_a} \right) \quad (4)$$

A. Models and assumptions

For the two presented estimators, it is assumed that the UAV is equipped with a standard sensor suite consisting of an inertial measurement unit (IMU), a GNSS receiver, and a heading reference such as a magnetometer. Furthermore, it is assumed that a biased relative velocity sensor is available. Such a sensor could be obtained by using the output of the pressure sensor-array approach presented in Borup et al. [5] treated as a virtual sensor. The measurements assumed are:

- An attitude estimate from an attitude estimator, typically in either Euler angles or quaternions, used to compute the rotation matrix $R_b^n(t)$. This estimate is assumed free of noise in the estimator design, but studied in simulation and experiments with added noise.
- A GNSS receiver velocity over ground measurement modeled by

$$v_{g,m}^n(t) = v_g^n(t) + \epsilon_{v_g} \quad (5)$$

where $\epsilon_{v_g} \sim \mathcal{N}(0, \Sigma_{v_g})$ is a noise term.

- An IMU specific force measurement modeled by

$$f_m^b(t) = f^b(t) + \epsilon_f \quad (6)$$

where $\epsilon_f \sim \mathcal{N}(0, \Sigma_f)$ is a noise term.

- An IMU angular rate measurement, compensated for bias and drift, modeled by

$$\omega_{b,m}(t) = \omega_b(t) + \epsilon_\omega \quad (7)$$

where $\omega_b(t) = [p(t), q(t), r(t)]^\top$ is the angular velocity of the BODY frame relative to the NED frame, decomposed in the BODY frame, and $\epsilon_\omega \sim \mathcal{N}(0, \Sigma_\omega)$ is a noise term.

- A biased relative velocity measurement such as the low-cost system [5] modeled by

$$v_{r,m}^b(t) = v_r^b + b^b + \epsilon_{v_r} \quad (8)$$

where $b^b = [b_u, b_v, b_w]^\top$ is a sensor bias and $\epsilon_{v_r} \sim \mathcal{N}(0, \Sigma_{v_r})$ is a noise term.

Note that the argument for time-varying signals have for the remainder of the article been omitted for notational simplicity, except when deemed essential for clarity. An example of a GES attitude and gyro bias observer is found in Grip et al. [11]. The bias-compensated IMU measurements of angular rate and specific force are only used in the relative velocity estimator. Similarly, the GNSS velocity measurement is only used in the relative velocity estimator, and only if wind velocity estimates are also desired.

For both estimators, it is assumed that the wind velocity vector field is slowly time-varying and uniform over the area of flight, i.e.

$$\dot{v}_w^n = \epsilon_{v_w} \quad (9)$$

where $\epsilon_{v_w} \sim \mathcal{N}(0, \Sigma_{v_w})$ is the wind model noise term, and that the relative velocity sensor bias is slowly time-varying

$$\dot{b}^b = \epsilon_b \quad (10)$$

where $\epsilon_b \sim \mathcal{N}(0, \Sigma_b)$ is the bias model noise term. These two model assumptions will be used in both the estimators and the states will be estimated using Kalman filters.

III. WIND VELOCITY ESTIMATOR

The wind velocity estimators presented in this section is inspired by the estimator presented in [13]. It estimates the wind velocity and the bias of the relative velocity sensor. Using the assumed measurements, it is possible from the wind velocity to estimate the relative velocity, and in turn the airspeed, AOA, and SSA. The structure of the wind velocity estimator is shown in Fig. 1.

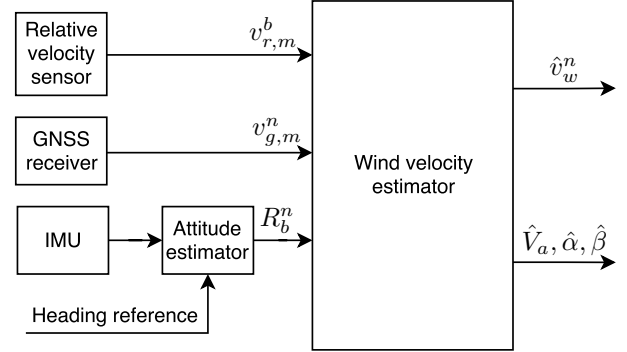


Fig. 1: Block diagram showing the cascaded structure of the wind velocity estimator.

By inserting the GNSS velocity over ground measurement and the relative velocity sensor measurement into Eq. 1, we get

$$v_{g,m}^n - R_b^n v_{r,m}^b = v_w^n + R_b^n b^b + R_b^n \epsilon_{v_r} + \epsilon_{v_g} \quad (11)$$

Consider the state vector

$$x_w = \begin{bmatrix} v_w^n \\ b^b \end{bmatrix}$$

and the composed measurement

$$y_w = v_{g,m}^n - R_b^n v_{r,m}^b$$

The linear system can be stated as

$$\dot{x}_w = G_w \epsilon_{x_w} \quad (12)$$

$$y_w = C_w(t) x_w + C_w(t) \epsilon_{y_w} \quad (13)$$

where

$$G_w = I_6, \quad \epsilon_{x_w} = \begin{bmatrix} \epsilon_{v_w} \\ \epsilon_b \end{bmatrix}$$

$$C_w(t) = [I_3 \quad R_b^n(t)], \quad \epsilon_{y_w} = \begin{bmatrix} \epsilon_{v_g} \\ \epsilon_{v_r} \end{bmatrix}$$

Also, notice that the system matrix is $A_w = 0_{6 \times 6}$.

A. Wind velocity estimator design

Consider the estimator

$$\dot{\hat{x}}_w = K_w (y_w - C_w \hat{x}_w) \quad (14)$$

where K_w is the Kalman filter gain matrix. The process noise covariance matrix is

$$Q_w = E[\epsilon_{x_w} \epsilon_{x_w}^\top] = Q_{x_w}$$

where $Q_{x_w} = \text{diag}(\Sigma_{v_w}, \Sigma_b)$. The measurement covariance matrix is found to be

$$\begin{aligned} R_w(t) &= E[C_w(t)\epsilon_{y_w}\epsilon_{y_w}^\top C_w(t)^\top] = C_w(t)E[\epsilon_{y_w}\epsilon_{y_w}^\top]C_w(t)^\top \\ &= C_w(t)R_{y_w}C_w(t)^\top \end{aligned}$$

where $R_{y_w} = \text{diag}(\Sigma_{v_g}, \Sigma_{v_r})$.

Proposition 1: Assume the angular velocity and angular acceleration of the UAV satisfies $\|\omega^b \times \dot{\omega}^b\| > 0$ for all $t \geq 0$, then the LTV system described by Eq. 12 and 13 is uniform completely observable (UCO) and uniform completely controllable (UCC).

Proof: First, we show UCO of the pair $(A_w, C_w(t))$. Theorem 6.O12 in Chen [7], states that the continuously differentiable pair $(A(t), C(t))$ is UCO at t , if there exists a finite $t_1 > t$ such that the observability codistribution $d\mathcal{O}_w = [N_0(t_1); \dots; N_{n-1}(t_1)]$ has full rank, where

$$N_0(t) = C(t)$$

$$N_{m+1}(t) = N_m(t)A(t) + \frac{d}{dt}N_m(t), \quad m = 0, 1, \dots, n-1$$

where n is the dimension of the state matrix. For the pair $(A_w, C_w(t))$, we have

$$\begin{aligned} d\mathcal{O}_w &= \begin{bmatrix} C_w(t) \\ \dot{C}_w(t) \\ \ddot{C}_w(t) \end{bmatrix} \\ &= \begin{bmatrix} I_3 & R_b^n(t) \\ 0_{3 \times 3} & R_b^n(t)S(\omega^b(t)) \\ 0_{3 \times 3} & R_b^n(t)S(\omega^b(t))^2 + R_b^n(t)S(\dot{\omega}^b(t)) \end{bmatrix} \end{aligned}$$

Given the form of $d\mathcal{O}_w$, to verify that it has full rank, it suffices to show that the submatrix

$$\mathcal{O}_{w,1} = [R_b^n(t)S(\omega^b(t))^2 + R_b^n(t)S(\dot{\omega}^b(t))]$$

is full rank, as proven by Meyer [22]. Since $R_b^n(t)$ is nonsingular, the conditions for which the codistribution $d\mathcal{O}_w$ is full rank corresponds to the conditions for which

$$[S(\omega^b)^2 + S(\dot{\omega}^b)]\zeta \neq 0 \quad \forall \|\zeta\| \neq 0 \quad (15)$$

where $\zeta \in \mathbb{R}^3$. Thus, the codistribution $d\mathcal{O}_w$ is not full rank if there exists $\zeta \neq 0$ such that

$$S(\omega^b)^2\zeta = -S(\dot{\omega}^b)\zeta \quad (16)$$

The skew-symmetric matrix functions as the cross product operator when post multiplied with a 3-dimensional vector, i.e. $S(x)y = x \times y$ for $y, x \in \mathbb{R}^3$. The two resulting vectors from $S(\omega^b)^2\zeta$ and $-S(\dot{\omega}^b)\zeta$ belong to two different subspaces of the vector space \mathbb{R}^3 that are both spanned by a line crossing through Origin, and the only common element of the two subspaces is the zero vector. The only solution to Eq. 16 is therefore

$$S(\omega^b)^2\zeta = -S(\dot{\omega}^b)\zeta = 0 \quad (17)$$

To see this, consider the following

$$S(\dot{\omega}^b)\zeta \in (\text{span}\dot{\omega}^b + \text{span}\zeta)^\perp =: \mathcal{A} \quad (18)$$

$$(\omega^b)^2\zeta \in (\text{span}\omega^b + (\text{span}\omega^b + \text{span})^\perp)^\perp =: \mathcal{B} \quad (19)$$

Since $S(\omega^b)^2\zeta = -S(\dot{\omega}^b)\zeta$, it implies that both $S(\omega^b)^2\zeta$ and $S(\dot{\omega}^b)\zeta$ belong to the same subspace $\mathcal{C} = \mathcal{A} \cap \mathcal{B}$. Then, observe that

$$\begin{aligned} \mathcal{C} &= (\mathcal{A}^\perp + \mathcal{B}^\perp)^\perp \\ &= (\text{span}\dot{\omega}^b + \text{span}\zeta + \text{span}\omega^b + (\text{span}\omega^b + \text{span}\zeta)^\perp)^\perp \\ &= \{0\} \end{aligned} \quad (20)$$

since $\text{span}\zeta + \text{span}\omega^b + (\text{span}\omega^b + \text{span}\zeta)^\perp = \mathbb{R}^3$.

Eq. 16 is easily seen to be true for $\omega^b = \dot{\omega}^b = 0$. Furthermore, if either ω^b or $\dot{\omega}^b$ is equal to zero, then choosing ζ to be collinear with the non-zero vector will result in both sides of the equality being zero. Moreover, for $\omega^b \neq 0$ and $\dot{\omega}^b \neq 0$, Eq. 16 is true when the vectors ζ , ω^b , and $\dot{\omega}^b$ are all collinear. Thus, the codistribution $d\mathcal{O}_w$ is full rank if $\dot{\omega}^b$ and ω^b are non-zero, noncollinear vectors, which corresponds to the requirement $\|\omega^b \times \dot{\omega}^b\| > 0$.

Lastly, it is easy to verify that the pair (A_w, G_w) is UCC.

■

The UCO and UCC properties of the system implies that the equilibrium points of the Kalman filter error dynamics, $\tilde{v}_w^n = v_w^n - \hat{v}_w^n$ and $\tilde{b}^b = b^b - \hat{b}^b$, are GES in the deterministic case, as proven by Anderson [3] and bounded in the mean-square sense in the stochastic case [12]. The definition of the estimator in Eq. 14 and the observability analysis is done in continuous time for convenience. However, the Kalman filter should be implemented using a discrete-time algorithm. The conducted analysis shows that in order for the system to be UCO, the requirement $\|\omega^b \times \dot{\omega}^b\| > 0$ has to be fulfilled. This correspond to a PE requirement on the angular rate, which needs to vary over time. The implications of this PE requirement is discussed in Section V and the estimator performances are investigated through a simulation study in Section VI and using experimental flight data in Section VII.

IV. RELATIVE VELOCITY ESTIMATOR

The relative velocity estimator is distinct from the wind velocity estimator. The estimator does not require velocity over ground measurements, but angular rate and specific force measurements. The relative velocity estimator structure is shown in Fig. 2.

The dynamics of the velocity over ground and attitude is described by

$$\dot{v}_g^n = R_b^n f^b + g^n \quad (21)$$

$$\dot{R}_b^n = R_b^n S(\omega^b) \quad (22)$$

where f^b is the specific force decomposed in the BODY frame and g^n is the gravity vector decomposed in the NED frame. Differentiating Eq. 1 results in

$$\dot{v}_g^n = R_b^n S(\omega^b)v_r^b + R_b^n \dot{v}_r^b + \epsilon_{v_w} \quad (23)$$

Inserting Eq. 21 into Eq. 23 and rearranging gives

$$\dot{v}_r^b = f^b + R_b^n g^n - S(\omega^b)v_r^b - R_b^n \epsilon_{v_w} \quad (24)$$

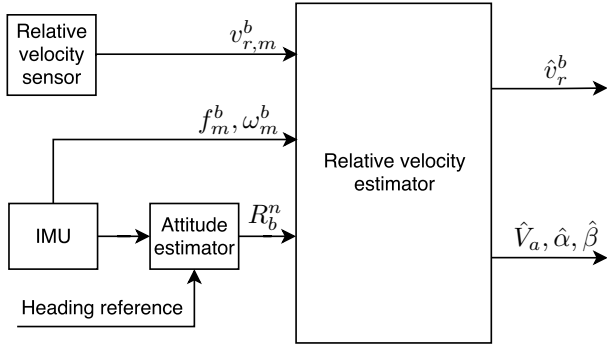


Fig. 2: Block diagram showing the cascaded structure of the relative velocity estimator.

Replacing the specific force and angular rate with the bias-compensated IMU measurements, we have that

$$\dot{v}_r^b = f_m^b + R_b^n g^n - S(\omega_m^b)v_r^b - \epsilon_f - S(v_r^b)\epsilon_\omega - R_b^n \epsilon_{v_w} \quad (25)$$

Consider the state vector

$$x_r = \begin{bmatrix} v_r^b \\ b^b \end{bmatrix} \quad (26)$$

and the input and measurement vector

$$u_r = \begin{bmatrix} f_m^b \\ g^n \end{bmatrix}, \quad y_r = v_{r,m}^b \quad (27)$$

Then the linear time-varying system can be stated as

$$\dot{x}_r = A_r(t)x_r + B_r(t)u_r + G_r(t, x_r)\epsilon_{x_r} \quad (28)$$

$$y_r = C_r x_r + \epsilon_{y_r} \quad (29)$$

where

$$A_r(t) = \begin{bmatrix} -S(\omega_m^b(t)) & 0_{3 \times 3} \\ 0_{3 \times 3} & 0_{3 \times 3} \end{bmatrix}, \quad B_r(t) = \begin{bmatrix} I_3 & (R_b^n(t))^T \\ 0_{3 \times 3} & 0_{3 \times 3} \end{bmatrix}$$

$$G_r(t, x_r) = \begin{bmatrix} -I_3 & -S(v_r^b(t)) & -(R_b^n(t))^T & 0_{3 \times 3} \\ 0_{3 \times 3} & 0_{3 \times 3} & 0_{3 \times 3} & I_3 \end{bmatrix}$$

$$\epsilon_{x_r} = \begin{bmatrix} \epsilon_f \\ \epsilon_\omega \\ \epsilon_{v_w} \\ \epsilon_b \end{bmatrix}, \quad C_r = [I_3 \quad I_3], \quad \epsilon_{y_r} = \epsilon_{v_r}$$

A. Relative velocity estimator design

Consider the estimator

$$\dot{\hat{x}}_r = A_r \hat{x}_r + B_r u_r + K_r (y_r - C_r \hat{x}_r) \quad (30)$$

where K_r is a time-varying Kalman gain. The process noise covariance matrix is

$$Q_r = E[G_r(t, \hat{x})\epsilon_{x_r}\epsilon_{x_r}^T G_r(t, \hat{x})^T] \\ = G_r(t, \hat{x})E[\epsilon_{x_r}\epsilon_{x_r}^T]G_r(t, \hat{x})^T \\ = G_r(t, \hat{x})Q_{x_r}G_r(t, \hat{x})^T$$

where $Q_{x_r} = \text{diag}(\Sigma_f, \Sigma_\omega, \Sigma_{v_w}, \Sigma_b)$. The measurement covariance matrix is

$$R_r = E[\epsilon_{y_r}\epsilon_{y_r}^T] = R_{y_r} \quad (31)$$

where $R_{y_r} = \Sigma_{v_r}$.

Proposition 2: Given the angular velocity and angular acceleration of the UAV satisfies $\|\omega^b \times \dot{\omega}^b\| > 0$ for all $t \geq 0$, then the LTV system described by Eq. 28 and 29 is UCO and UCC.

Proof: We start by showing UCO of the pair $(A_r(t), C_r)$ as defined for the LTV system described by Eq. 28 and 29. Once again employing Theorem 6.O12 of Chen [7], we have

$$d\mathcal{O}_r = \begin{bmatrix} C_r \\ C_r A_r(t) \\ C_r A_r(t)^2 + C_r \dot{A}_r(t) \end{bmatrix} \\ = \begin{bmatrix} I_3 & I_3 \\ -S(\omega^b(t)) & 0_{3 \times 3} \\ S(\omega^b(t))^2 - S(\dot{\omega}^b(t)) & 0_{3 \times 3} \end{bmatrix}$$

By the same argumentation used in the proof for Proposition 1, full rank of the observability codistribution $d\mathcal{O}_r$ is obtained if $\dot{\omega}^b$ and ω^b are non-zero, noncollinear vectors, which corresponds to the requirement $\|\omega^b \times \dot{\omega}^b\| > 0$.

Lastly, we show that the pair $(A_r(t), G_r)$ is UCC. Theorem 6.12 of Chen [7], states that the continuously differentiable pair $(A(t), G(t))$ is UCC at t_0 if there exists a finite $t_1 > t_0$ such that the controllability codistribution $d\mathcal{C}_r = [M_0(t), \dots, M_{n-1}(t)]$ has full rank, where

$$M_0(t) = G(t)$$

$$M_{m+1}(t) = -A(t)M_m(t) + \frac{d}{dt}M_m(t)$$

Applying the theorem it is sufficient to examine the first set of columns of controllability codistribution $C_r = M_0 = G_r(t)$, where it is easy to see that this has full rank. ■

The UCO and UCC properties of the system implies that the equilibrium points of the Kalman filter error dynamics, $\tilde{v}_r^b = v_r^b - \hat{v}_r^b = 0$ and $\tilde{b}^b = b^b - \hat{b}^b = 0$, are GES in the deterministic case, as proven by Anderson [3] and bounded in the mean-square sense in the stochastic case [12]. Similar to wind velocity estimator, the definition of the relative velocity estimator in Eq. 30 and the observability analysis is done in continuous time for convenience.

V. PERSISTENCE OF EXCITATION REQUIREMENT

The presented wind velocity and relative velocity estimators have been proven to have favorable estimation properties if the requirement $\|\omega^b \times \dot{\omega}^b\| > 0$ is fulfilled for $t \geq 0$. As stated previously, this corresponds to the angular rate and angular acceleration vectors, ω^b and $\dot{\omega}^b$, being non-zero and linearly independent. The requirement on the angular acceleration means that a constant rotation around any axis of the UAV, does not provide PE. Similarly, an angular acceleration around a single axis of the BODY frame with no angular velocity around a different axis, will results in a zero-valued cross product between the two vectors. To achieve PE, the UAV will therefore have to engage in a flight pattern that causes at least two of the angular rate vector components to be non-zero and

one of those components to vary over time. As an example, this could be accomplished by flying in a sinusoidal or figure-eight course pattern, where both roll, pitch, and yaw angles of the UAV are continuously changing. The PE requirement could appear to be a disadvantage to the presented method, since imposing requirements on the operational behavior of the UAV could oppose the interests of the UAV operator. However, the presented estimators could be augmented with a simple module that determines whether the level of PE is sufficient to update the estimates combined with a take-off trajectory that ensures a long enough period with proper PE to have converged bias estimates, before continuing with the operation flight trajectory. Lastly, it should also be noted that PE is a theoretical concept, and the requirements on the level of excitation needed for convergence will in practice be governed by many different factors such as noise levels on sensors, validity of the system model, along with other error sources.

VI. SIMULATION STUDY

This section presents simulation results for the wind velocity estimator and the relative velocity estimator. The results are obtained using the UAV model presented in Beard and McLain [4] with the Aerosonde UAV model parameters. Since both estimators are based on kinematics, the aerodynamic model of the UAV does not influence the estimation properties of the estimators.

The wind is modeled as a uniform constant wind field with added turbulence. The turbulence is generated as white noise filtered through a Dryden model, with the transfer functions

$$H_u(s) = \sigma_u \sqrt{\frac{2V_a}{L_u}} \frac{1}{s + V_a/L_u} \quad (32)$$

$$H_v(s) = \sigma_v \sqrt{\frac{3V_a}{L_v}} \frac{(s + V_a/(\sqrt{3}L_v))}{(s + V_a/L_u)^2} \quad (33)$$

$$H_w(s) = \sigma_w \sqrt{\frac{3V_a}{L_w}} \frac{(s + V_a/(\sqrt{3}L_w))}{(s + V_a/L_w)^2} \quad (34)$$

where σ_u , σ_v , σ_w and L_u , L_v , L_w are the turbulence intensities and spatial wavelengths along the vehicle frame axes as defined in [23]. The simulation assumes low altitudes and moderate gusts. Suitable Dryden model parameter values for these conditions was presented by Langelaan et al. [14] and the Dryden model has been implemented with those given parameters values and a constant nominal airspeed $V_a = V_{a0}$. The parameter values are listed in Table I.

| | | |
|----------------------|------|-----|
| altitude | 50 | m |
| L_u, L_v | 200 | m |
| L_w | 50 | m |
| σ_u, σ_v | 2.12 | m/s |
| σ_w | 1.4 | m/s |
| V_{a0} | 26 | m/s |

TABLE I: Dryden gust model parameters used in simulation.

The simulated trajectory has been chosen to provide insight into the behavior of the two estimators with respect to PE requirements. The simulation is initiated with trim conditions at an altitude of 50 m and an airspeed of 26 m/s. After 50 seconds, the course control command objective is chosen as a sinusoidal signal with amplitude of 50 degrees and a frequency of 0.04 Hz. This course control command pattern is continued for 100 seconds, corresponding to four periods. At time 225 s to 325 s, the altitude objective was similarly chosen as a sinusoidal signal with an amplitude of 10 m and a frequency of 0.04 Hz. It is worth noticing that the wind influence on the UAV, will result in a non-perfect tracking of control objectives. Plots of the position, angular rates, and Euler angles obtained through simulations are shown in figures 3 - 5. The angular rates indicate that the PE assumption of $\|\omega^b \times \dot{\omega}^b\| > 0$ only holds between time 50 s to time 150 s, i.e. when the course control signal command is varied.

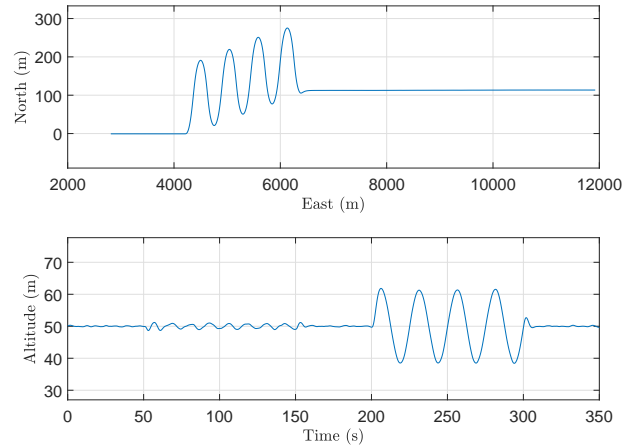


Fig. 3: The trajectory described by the UAV in simulation.

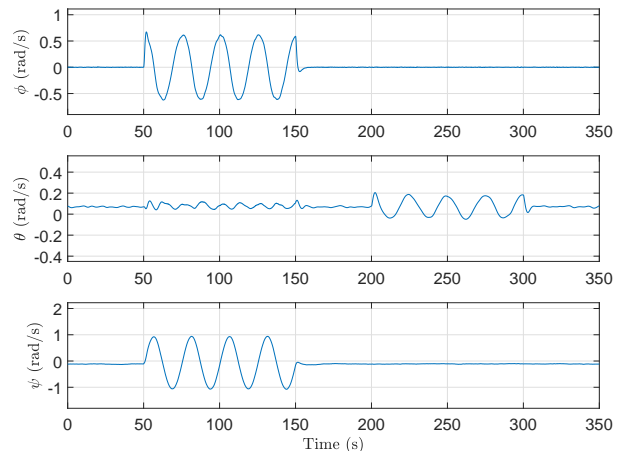


Fig. 4: The Euler angles obtained from simulations.

For both estimators, the sensors were assumed corrupted by additive, uncorrelated, zero-mean white noise and sampled

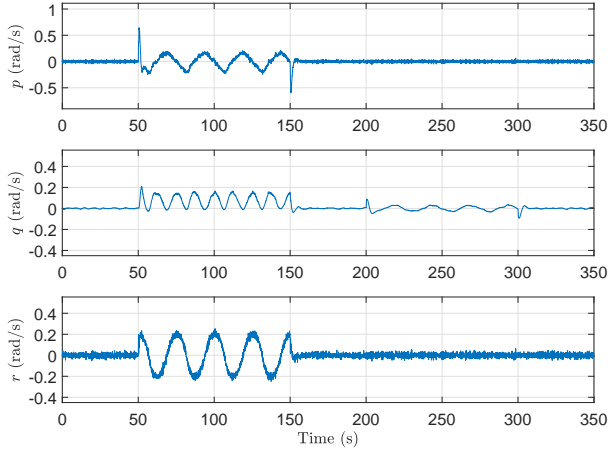


Fig. 5: The angular rates obtained from simulation.

at 100Hz. For the biased relative velocity measurement, a standard deviation of 0.05 m/s was applied and an arbitrarily chosen constant bias $b = [2.0, -1.5, 1.3]$ was added. The rotation matrix was parametrized by Euler angles with a white noise term with standard deviation 1.0 deg. For the wind velocity estimator, the GNSS velocity over ground measurement white noise term was assumed to have a standard deviation of 0.05 m/s, and for the relative velocity estimator, the specific force measurements and the angular rate measurements were assumed to have white noise terms with standard deviations of 2.5×10^{-3} deg/s and 2.5×10^{-3} m/s².

A. Wind velocity estimator simulation results

For the wind velocity estimator, the wind model noise standard deviations were chosen by tuning as $\Sigma_{v_w} = 1 \times 10^{-2} I_3$, and the bias model noise standard deviations were chosen by tuning as $\Sigma_b = 1 \times 10^{-4} I_3$, and the error covariance matrix was initialized as $P_{w,0} = 1 \times 10^{-2} I_6$. The tuning was chosen with a prioritization of steady state performance over fast convergence. The simulation results are shown in Fig. 6 - 8.

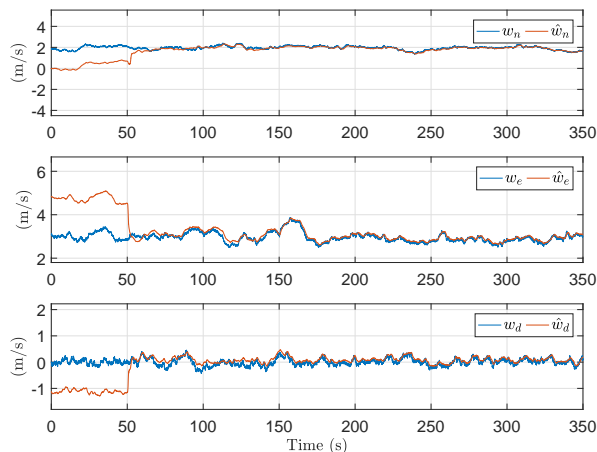


Fig. 6: The wind velocity obtained from simulation using the Dryden wind model and the corresponding wind velocity estimator estimates.

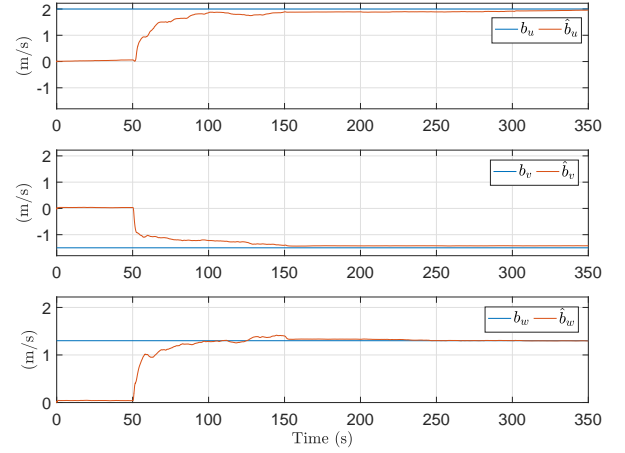


Fig. 7: The relative velocity sensor bias and the wind velocity estimator bias estimates.

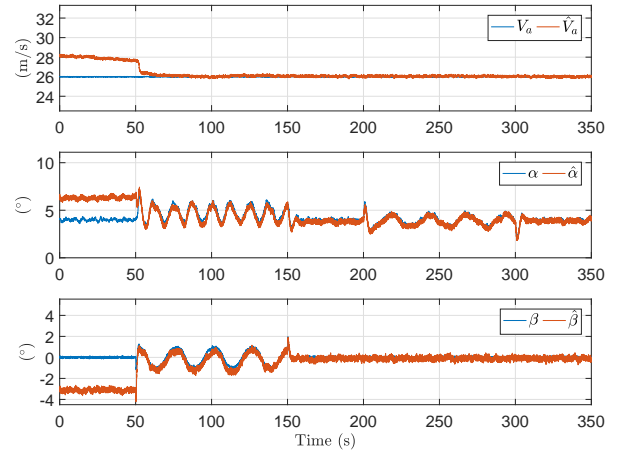


Fig. 8: The air data obtained from simulation and the air data estimates computed from the wind velocity estimator.

The results show that during the first 50 seconds of trim flight conditions, the wind velocity estimator is not provided with sufficient PE and the estimates do not converge. Once the UAV engages in a sinusoidal course pattern, the estimates converge to the true values. After convergence, there is no divergence even in periods without PE. RMSE results from the period after $t = 100$ seconds is shown in table II.

| | | |
|---------------|------|-----|
| \tilde{v}_n | 0.07 | m/s |
| \tilde{v}_e | 0.09 | m/s |
| \tilde{v}_d | 0.10 | m/s |
| \tilde{b}_u | 0.07 | m/s |
| \tilde{b}_v | 0.08 | m/s |
| \tilde{b}_w | 0.09 | m/s |

TABLE II: The RMSE obtained from simulation for the wind velocity estimator after $t = 100$ seconds.

B. Relative velocity estimator simulation results

For the relative velocity estimator, the wind model noise standard deviations, the bias model noise standard deviations, and the initial error covariance matrix were chosen as the same values as used in the wind velocity estimator simulation. The simulation results are shown in Fig. 9 - 11.

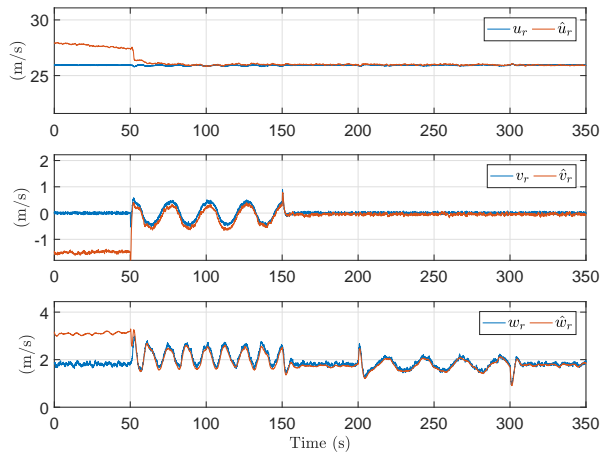


Fig. 9: The relative velocity obtained from simulation and the corresponding relative velocity estimator estimates.

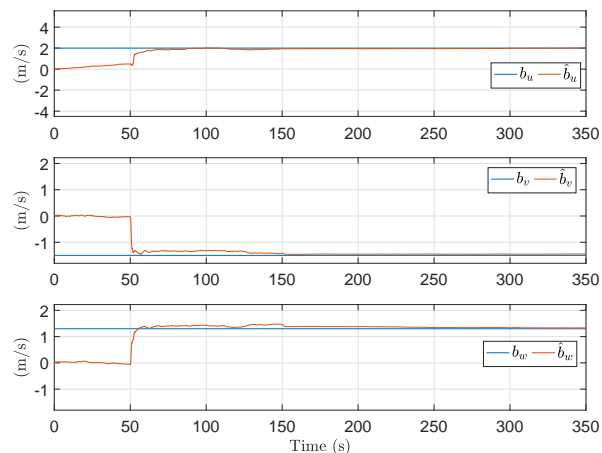


Fig. 10: The relative velocity sensor bias and the relative velocity estimator bias estimates in simulation.

Similarly to the wind velocity estimator, the relative velocity estimator does not show convergence of estimates for the first 50 seconds. After the UAV initiates the sinusoidal course pattern, the estimates start converging towards the true values and does not diverge in the following periods without PE. RMSE results from the simulation period after 100 seconds are shown in table III.

VII. EXPERIMENTAL FLIGHT TEST RESULTS

This section contains results from testing the air data system bias correction estimators on experimental flight data. The flight data was obtained on the 30th of January, 2017,

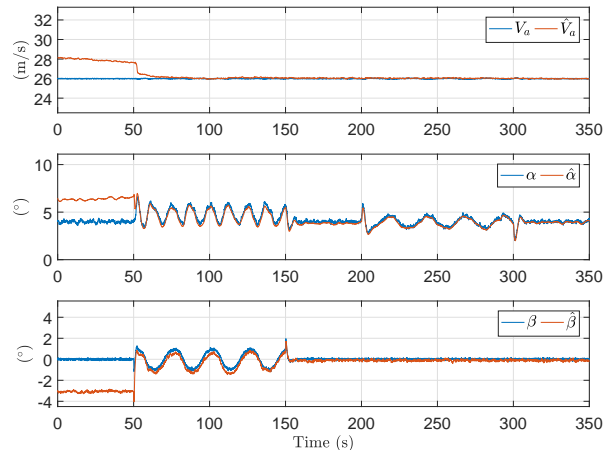


Fig. 11: The air data obtained from simulation and the air data estimates computed from the relative velocity estimator.

| | | |
|---------------|------|-----|
| \tilde{u}_r | 0.07 | m/s |
| \tilde{v}_r | 0.08 | m/s |
| \tilde{w}_r | 0.09 | m/s |
| \tilde{b}_u | 0.06 | m/s |
| \tilde{b}_v | 0.07 | m/s |
| \tilde{b}_w | 0.08 | m/s |

TABLE III: The RMSE obtained from simulation for the relative velocity estimator after $t = 100$ seconds.

outside of Agdenes in Norway using a Skywalker X8 Flying Wing UAV. The Skywalker X8 is a consumer grade UAV with a wingspan of 2.12 m that is usually flown in airspeeds ranging from 15-25 m/s. A picture of the Skywalker X8 UAV in flight is shown in Fig. 12.



Fig. 12: A Skywalker X8 in flight. Copyright: João Fortuna, NTNU.

A STIM300 IMU was used to provide angular rate and specific force measurements at 500 Hz. The pressure sensor-array approach presented in Borup et al. [5] has been used as a virtual relative velocity sensor. The approach revolves around combining an array of Bosch BMP280 sensors embedded in the surface of the airframe of the UAV with either neural network or linear regression algorithms. For these results, three neural networks were trained to provide each of the three components of the relative velocity virtual sensor measurements at 20 Hz. Given the use of low-cost off-the-shelf components, the system in [5] is inexpensive

compared to commercially available solutions. However, the estimators presented in this article are not limited to using this system, but instead to any air data system providing relative velocity measurements that has a constant or slowly time-varying bias. As a ground truth reference, the Micro Air Data System by the Aeroprobe Corporation has been used to provide relative velocity measurements at 100 Hz. The sensor measurements has been logged with an accurate timing of less than 10 ns using the SyncBoard [2]. In addition, a Pixhawk PX4 Autopilot was used to provide EKF attitude and velocity over ground estimations. The estimators are tested on a flight segment that is 10 minutes long. The relative velocity virtual sensor measurements and the ground truth values are shown in Fig. 13 and 14. It is evident that the virtual sensor does not output a perfectly biased relative velocity measurement, but it does appear to capture the high-frequency dynamics. The bias errors in the neural network outputs are assumed to be attributed to one of two things. The BMP280 sensors are subjects to a slowly time-varying drift that a pre-flight calibration process is used to compensate for. This calibration uses the mean of the BMP280 sensor measurements for a shorter period and noise from wind during this process will negatively influence the results. In addition, [5] assumes that the pressure distribution, given enough data, is invariant to ambient conditions, and the amount of data used to train the NNs may not be sufficient.

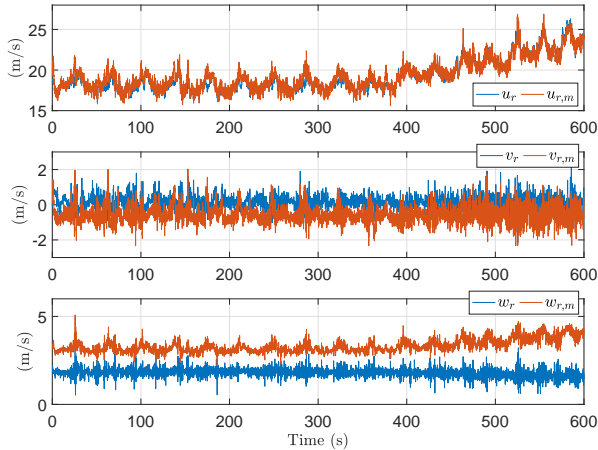


Fig. 13: The relative velocity virtual sensor measurements and the Micro Air Data System ground truth values. It appears that there are biases between the two sets of signals and that these biases are slowly time-varying.

The flight is spent loitering in a circle with an approximate radius of 100 m, where better PE conditions probably could have been achieved with sinusoidal patterns or figure-eight flying. However, the yaw rate appears to behave in a sinusoidal fashion which corresponds to a non-zero angular acceleration component and both the pitch and yaw rates also appears to deviate from zero at times. The position, angular rates, and Euler angles are shown in Fig. 15 - 17. Also, note that the mounting of the Micro Air Data System probe on the Skywalker UAV is a potential error source, since an error in

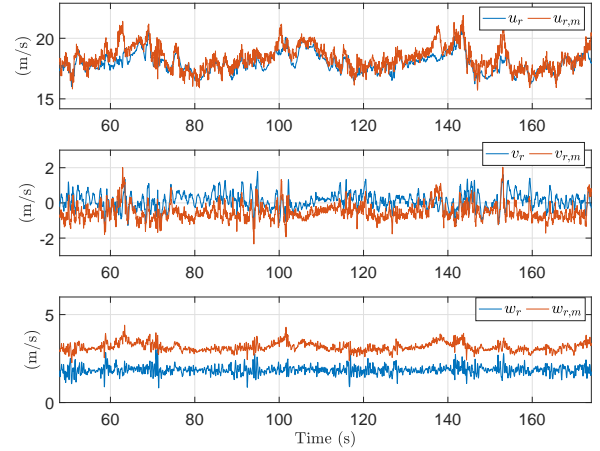


Fig. 14: A closer look at the virtual sensor relative velocity measurements and the ground truth values.

the alignment of the probe with respect to the definitions of the virtual relative velocity sensor axes will result in estimation errors.

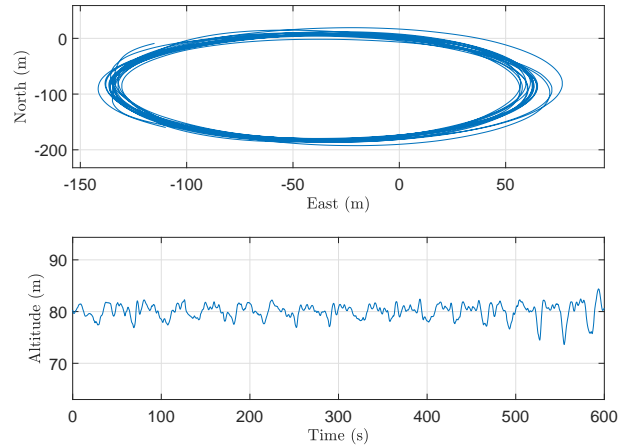


Fig. 15: The trajectory described by the UAV during the experimental flight.

A. Wind velocity estimator flight results

For the experimental flight data, the wind velocity estimator was tuned as $\Sigma_{v_w} = \text{diag}(3 \times 10^{-2}, 3 \times 10^{-2}, 8 \times 10^{-2})$, and $\Sigma_b = 9 \times 10^{-6} I_3$. The error covariance matrix was initialized as $P_{w,0} = \text{diag}(3 \times 10^{-5}, 3 \times 10^{-6}, 3 \times 10^{-4}, 3 \times 10^{-4})$. The sensor noise covariance matrices were chosen by tuning as $\Sigma_{v_g} = \text{diag}(1 \times 10^{-2}, 1 \times 10^{-2}, 2 \times 10^{-2})$ and $\Sigma_{v_r} = \text{diag}(6 \times 10^{-3}, 6 \times 10^{-3}, 3 \times 10^{-3})$. The tuning was conducted with a prioritization of steady state performance over fast convergence. The experimental flight test results are shown in Fig. 18 - 20. The wind velocity estimator RMSE results from the flight after the initial 100 seconds have passed are listed in table IV.

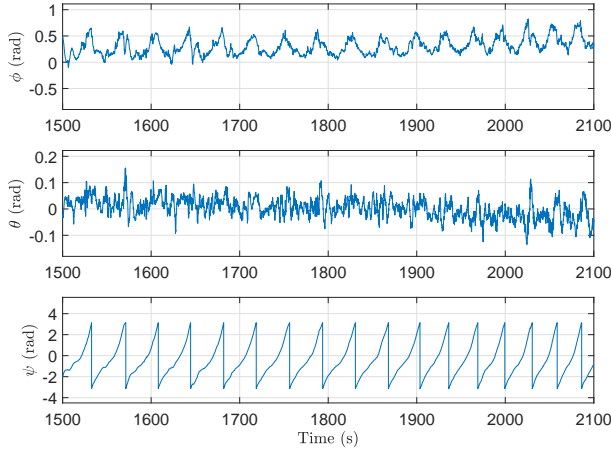


Fig. 16: The Euler angles obtained from the Pixhawk PX4 Autopilot during the experimental flight test.

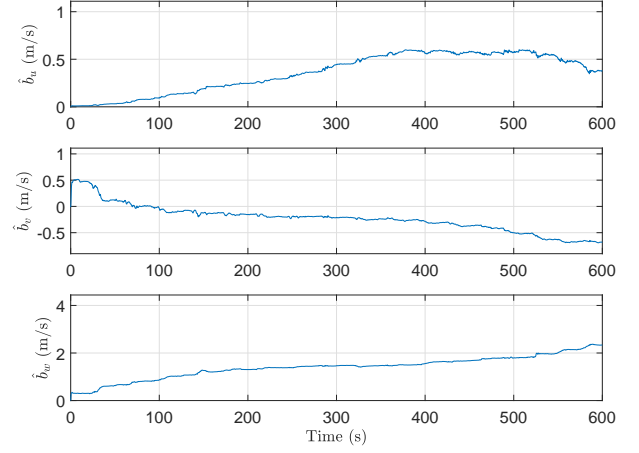


Fig. 19: The relative velocity sensor bias estimates from the wind velocity estimator.

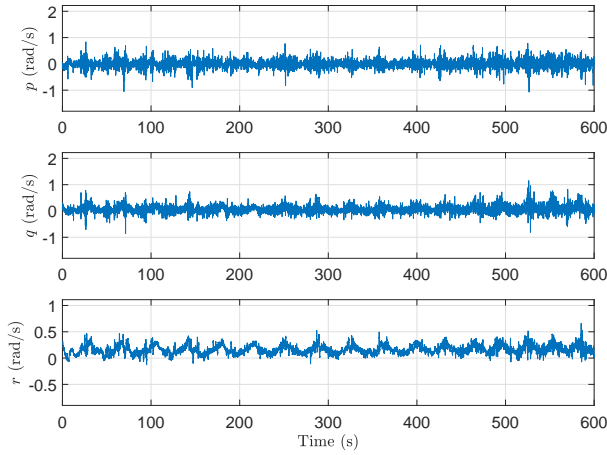


Fig. 17: The angular rates obtained from the STIM300 IMU during the experimental flight test. It is not obvious whether the angular rates and angular acceleration from this test flight provides sufficient PE for the estimators to have UCO properties.

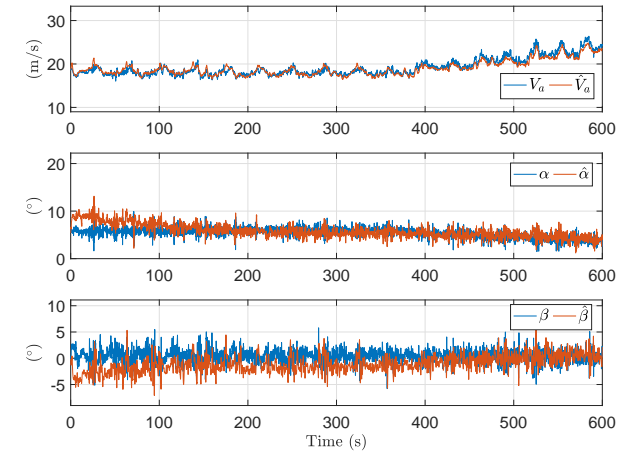


Fig. 20: The air data obtained from experimental flight and the air data estimates computed from the wind velocity estimator estimates.

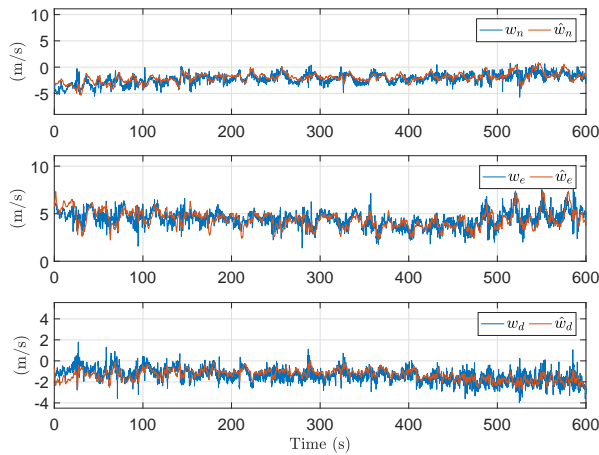


Fig. 18: The wind velocity computed from from the Micro Air Data System using the relations in Eq. 1 and the wind velocity estimates from the wind velocity estimator.

| | | |
|------------------|------|-----|
| \bar{V}_a | 0.69 | m/s |
| $\tilde{\alpha}$ | 1.14 | deg |
| $\tilde{\beta}r$ | 2.24 | deg |
| \tilde{v}_n | 0.73 | m/s |
| \tilde{v}_e | 0.68 | m/s |
| \tilde{v}_d | 0.44 | m/s |

TABLE IV: The RMSE obtained from flight data for the wind velocity estimator after $t = 100$ seconds.

B. Relative velocity estimator flight results

For the experimental flight data, the relative velocity estimator was initialised with the same values for the wind model noise, the bias model noise, the error covariance matrix, and the velocity sensor error covariance as the wind velocity estimator was. The sensor noise covariance matrices were chosen by tuning as $\Sigma_f = 1 \times 10^{-2} I_3$, and $\Sigma_\omega = 1 \times 10^{-3} I_3$. The tuning was conducted with a prioritization of steady state performance over fast convergence. The experimental flight

test results are shown in Fig. 21 - 23. The wind velocity estimator RMSE results from the flight after the initial 100 seconds have passed are listed in table V.

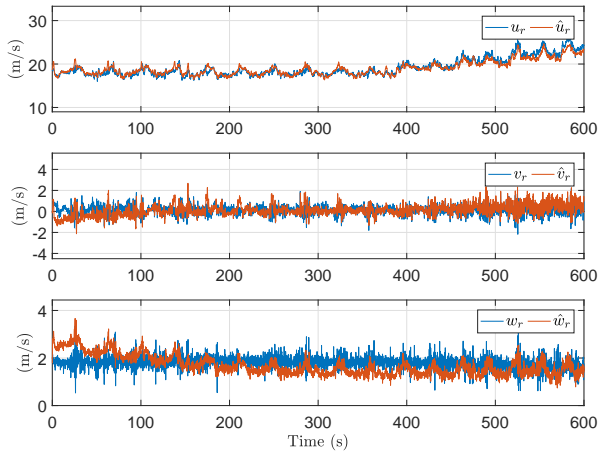


Fig. 21: The relative velocity obtained from the Micro Air Data System and the relative velocity estimator estimates.

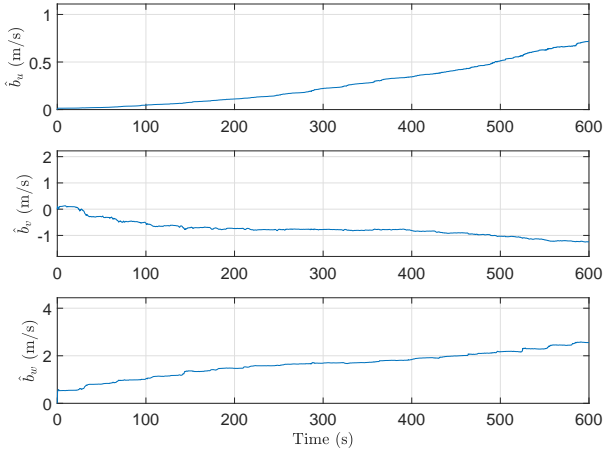


Fig. 22: The relative velocity sensor bias estimates from the relative velocity estimator.

| | | |
|-------------------|------|-----|
| \tilde{V}_a | 0.71 | m/s |
| $\tilde{\alpha}$ | 1.23 | deg |
| $\tilde{\beta}_r$ | 1.25 | deg |
| \tilde{u}_r | 0.70 | m/s |
| \tilde{v}_r | 0.43 | m/s |
| \tilde{w}_r | 0.41 | m/s |

TABLE V: The RMSE obtained from flight data for the relative velocity estimator after $t = 100$ seconds.

C. Discussion

The experimental results show that the estimates of both the wind velocity and relative velocity estimators convergence toward the ground truth values. However, the convergence

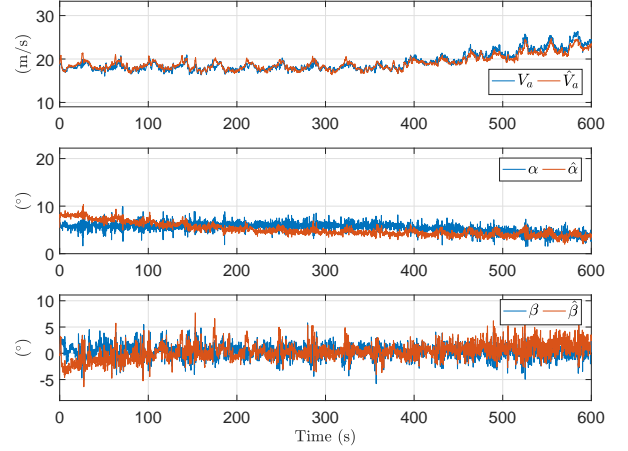


Fig. 23: The air data obtained from experimental flight and the air data estimates computed from the relative velocity estimator estimates.

appears to be slow and with a limit on the level of obtainable estimation accuracy. The limited accuracy is assumed to be caused by several factors. As previously noted, the level of PE could have been higher, e.g. if the aircraft had engaged in figure-eight flying patterns where the pitch and roll rates would have been further excited. Obviously, a PE requirement is a theoretical concept and for the experimental flight data, the level of PE may be relatively low when compared to the influences from other error sources. The simulation results presented in Section VI showed a higher accuracy of the two estimators and the error sources from implementing the estimators in practice appear to reduce the estimation accuracy.

An important error source to consider, is the influence of attitude estimation errors on the results. Both estimators assume to be provided with an attitude estimate as described in Section VI. This attitude estimate is used in converting between the BODY and NED frames for signals and noise propagation. Errors in the attitude estimates therefore results in errors in the state estimation of the two estimators. Furthermore, for the wind velocity estimator, the attitude estimate is also used to provide the wind velocity ground truth signal. Comparing this wind velocity ground truth signal to the Dryden wind model signal used in simulation, the wind speed variance is found to be more than 70 times higher. This significant increase in wind speed variance will have a negative effect on the estimation accuracy since the wind is assumed to be slowly time-varying. The high variance is assumed to be caused by windy conditions during the experiments, but errors in the attitude estimates and ground truth sensor noise are also assumed to have a significant influence.

Neither estimator has air data parameters as states and the results shown in Fig. 20 and 23 have been calculated based on the the estimators respective states. Comparing the numeric results of the two estimators can be misleading since the Kalman filter tuning will influence the output of the estimators. However, the results presented in Table IV and V, indicates no significant advantage of one estimator over the

other with respect estimation accuracy for airspeed and AOA, with the wind velocity estimator having higher accuracy in SSA estimation. For high-performance flight, the knowledge of AOA is critical to avoid unsafe conditions and to operate as close to the margins as possible. An AOA estimation accuracy of 1.2-1.3 degrees can be argued to be sufficient for this purpose, since stall-preventive safety margins are typically larger.

Besides the biased relative velocity measurements and attitude estimates, the wind velocity estimator relies on position measurements from a GNSS receiver, where the relative velocity estimator instead uses specific force and angular rate measurements from an IMU. The accuracy of the payload sensors will influence the results of the estimators and could result in one estimator providing higher accuracy estimates than the other, e.g. if the aircraft payload contains an expensive, high-precision IMU, then there is a possibility that the relative velocity estimator could outperform the wind velocity estimator. It is also possible to use both estimators in parallel. This structure would open up for a fault detection and isolation structure and this could be used to increase robustness of the UAV.

VIII. CONCLUSION

In this paper, two different Kalman filter approaches for correcting air data systems for a constant or slowly time-varying error bias were presented. The estimators are designed for fixed-wing unmanned aerial vehicles and use a standard sensor suite consisting of a GNSS receiver, an IMU, and a heading reference, combined with an air data system that is assumed to provide measurements with an unknown additive slowly time-varying bias. The proposed estimators are not aircraft model-dependent and are in the absence of noise proven to have globally exponentially stable equilibrium points for the error dynamics if provided with persistence of excitation of the angular rates of the unmanned aircraft. The estimators are verified through simulation and using experimental flight data. The experimental data indicates that a certain amount of PE is necessary to provide converging estimates for turbulent wind conditions.

ACKNOWLEDGMENT

This work was supported by the Norwegian Research Council (grant no. 221666, 223254 and 261791) through the Center of Autonomous Marine Operations and Systems (NTNU AMOS) and FORNY (project no. 90189003) at the Norwegian University of Science and Technology. The authors are very thankful for the SyncBoard provided by Sigurd Albrektsen at NTNU and effort of the skilled pilots here at NTNU, Lars Semb and Pål Kvaløy, who flew the Skywalker X8 for the experimental flight data set. In addition, a thanks to Andreas Wenz for the collaboration in data collecting.

REFERENCES

- [1] Aeroprobe. Micro Air Data System [measurement system]. Available from <http://www.aeroprobe.com/micro-air-data-computer-models/>.
- [2] S. M. Albrektsen and T. A. Johansen. SyncBoard - A high accuracy sensor timing board for UAV payloads. In *2017 International Conference on Unmanned Aircraft Systems (ICUAS)*, 2017.
- [3] B. D. O. Anderson. Stability Properties of Kalman-Bucy Filters. *Journal of the Franklin Institute*, vol. 2, pp. 137-144, 1971.
- [4] R. W. Beard and T. W. McLain. *Small Unmanned Aircraft - Theory and Practice*. Princeton University Press, 2012.
- [5] K. T. Borup, T. I. Fossen, and T. A. Johansen. A Machine Learning Approach for Estimating Air Data Parameters for Small Fixed-Wing UAVs Using Distributed Pressure Sensors. Submitted to IEEE Transactions on Aerospace and Electronic Systems. A preprint is available [here](#).
- [6] S. Callegari, A. Talamelli, M. Zagnoni, A. Golfarelli, V. Rossi, M. Tartagni, and E. Sangiorgi. Aircraft Angle of Attack and Air Speed Detection by Redundant Strip Pressure Sensors. *SENSORS, 2004 IEEE*, 2004.
- [7] C. Chen. *Linear System Theory and Design, 4th ed.* Oxford University Press, 2013.
- [8] A. Cho, Y. Kang, B. Park, and C. Yoo. Airflow angle and wind estimation using GPS/INS navigation data and airspeed. In *2013 13th International Conference on Control, Automation and Systems (ICCAS)*, 2013.
- [9] Flying. Qualities of Piloted Aircraft. Technical report, United States of America Department of Defense, 1995.
- [10] B. Girardet, L. Lapasset, D. Delahaye, and C. Rabut. Wind-Optimal Path Planning: Application to Aircraft Trajectories. In *13th International Conference on Control Automation Robotics and Vision, ICARCV 2014*, 2014.
- [11] H. F. Grip, T. I. Fossen, T. A. Johansen, and A. Saberi. Globally exponentially stable attitude and gyro bias estimation with application to GNSS/INS integration. *Automatica*, vol. 51, pp. 158-166, 2015.
- [12] A. H. Jazwinski. *Stochastic Processes and Filtering Theory*. Academic Press, 1970.
- [13] T. A. Johansen, A. Cristofaro, K. L. Sørensen, J. M. Hansen, and T. I. Fossen. On estimation of wind velocity, angle-of-attack and sideslip angle of small UAVs using standard sensors. In *2015 International Conference on Unmanned Aircraft Systems (ICUAS)*, 2015.
- [14] Jack W. Langelaan, Nicholas Alley, and James Neidhoefer. Wind Field Estimation for Small Unmanned Aerial Vehicles. *Journal of Guidance, Control, and Dynamics*, vol. 34, pp. 1016-1030, 2011.
- [15] T. J. Larson and P. M. Siemers III. Subsonic Tests of an All-Flush-Pressure-Orifice Air Data System. *NASA TP-1871*, 1981.
- [16] T. J. Larson, S. A. Whitmore, L. J. Ehernberger, J. B. Johnson, and P. M. Siemers III. Qualitative Evaluation of a Flush Air Data System at Transonic Speeds and High Angles of Attack. *NASA TP-2716*, 1987.
- [17] F. A. P. Lie and D. Gebre-Egziabher. Synthetic Air Data System. *Journal of Aircraft*, vol. 50, pp. 1234-1249, 2013.
- [18] H. Long and S. Song. Method of estimating angle-of-attack and sideslip angle based on data fusion. In *2009*

- 2nd International Conference on Intelligent Computing Technology and Automation*, 2009.
- [19] S. H. Mathisen, V. Grindheim, and T. A. Johansen. Approach Methods for Autonomous Precision Aerial Drop from a Small Unmanned Aerial Vehicle. *IFAC-PapersOnLine*, 2017.
- [20] S. H. Mathisen, K. Gryte, T. I. Fossen, and T. A. Johansen. Non-linear Model Predictive Control for Longitudinal and Lateral Guidance of a Small Fixed-Wing UAV in Precision Deep Stall Landing. In *AIAA Infotech @ Aerospace*, 2016.
- [21] M. Merz and T. A. Johansen. Optimal Path of a UAV Engaged in Wind-influenced Circular Towing. In *RED-UAS*, 2017.
- [22] C. D. Meyer Jr. Generalized Inverses and Ranks of Block Matrices. *SIAM Journal on Applied Mathematics*, vol. 25, pp 591-6002, 1973.
- [23] D. J. Moorhouse and R. J. Woodcock. MIL-F-8785C. Technical report, Air Force Research Laboratory - Wright-Patterson Air Force Base, 1982.
- [24] D. R. Nelson, D. B. Barber, T. W. McLain, and R. W. Beard. Vector Field Path Following for Miniature Air Vehicles. *IEEE Transactions on Robotics*, vol. 23, pp. 519-529, 2007.
- [25] J. Quindlen and J. Langelaan. Flush Air Data Sensing for Soaring-Capable UAVs. In *51st AIAA Aerospace Sciences Meeting including the New Horizons Forum and Aerospace Exposition*, 2013.
- [26] C. Ramprasadh and H. Arya. Multistage-Fusion Algorithm for Estimation of Aerodynamic Angles in Mini Aerial Vehicle. *Journal of Aircraft*, vol. 49, pp. 93-100, 2012.
- [27] A. Ray and R. Luck. An introduction to sensor signal validation in redundant measurement systems. *IEEE Control Systems Magazine*, vol. 11, pp. 44-49, 1991.
- [28] M. B. Rhudy, M. L. Fravolini, Y. Gu, M. R. Napolitano, S. Gururajan, and H. Chao. Aircraft model-independent airspeed estimation without pitot tube measurements. *IEEE Transactions on Aerospace and Electronic Systems*, vol. 51, pp. 1980-1995, 2015.
- [29] T. J. Rohloff, S. A. Whitmore, and I. Catton. Fault-Tolerant Neural Network Algorithm for Flush Air Data Sensing. *Journal of Aircraft*, 36(3):541-549, may 1999.
- [30] T. J. Rohloff, S. A. Whitmore, and I. Catton. Air Data Sensing from Surface Pressure Measurements Using a Neural Network Method. *AIAA Journal*, vol. 36, pp. 2094-2101, 1998.
- [31] I. Samy, I. Postlethwaite, D. Gu, and J. Green. Neural-Network-Based Flush Air Data Sensing System Demonstrated on a Mini Air Vehicle. *Journal of Aircraft*, vol. 47, pp. 18-31, 2010.
- [32] K. L. Sørensen, M. Blanke, and T. A. Johansen. Diagnosis of Wing Icing Through Lift and Drag Coefficient Change Detection for Small Unmanned Aircraft. In *Safeprocess*, 2015.
- [33] A. Wenz and T. A. Johansen. Estimation of Wind Velocities and Aerodynamic Coefficients for UAVs using standard Autopilot Sensors and a Moving Horizon Estimator. In *2017 International Conference on Unmanned Aircraft Systems (ICUAS)*, 2017.
- [34] A. Wenz, T. A. Johansen, and A. Cristofaro. Combining model-free and model-based Angle of Attack estimation for small fixed-wing UAVs using a standard sensor suite. In *2016 International Conference on Unmanned Aircraft Systems (ICUAS)*, 2016.
- [35] S. A. Whitmore, R. J. Davis, and J. Fife. In-flight demonstration of a real-time flush airdata sensing system. *Journal of Aircraft*, vol. 33, pp. 970-977, 1996.